

# Mean and Unsteady Flow Reconstruction Using Data-Assimilation and Resolvent Analysis

Sean Symon\*

California Institute of Technology, Pasadena, California 91125

Denis Sipp<sup>†</sup>

ONERA–The French Aerospace Lab, 92190 Meudon, France

Peter J. Schmid<sup>‡</sup>

Imperial College London, London, England SW7 2AZ, United Kingdom

and

Beverley J. McKeon<sup>§</sup>

California Institute of Technology, Pasadena, California 91125

DOI: 10.2514/1.J057889

A methodology is presented that exploits both data-assimilation techniques and resolvent analysis for reconstructing turbulent flows, containing organized structures, with an efficient set of measurements. The mean (time-averaged) flow is obtained using variational data-assimilation that minimizes the discrepancy between a limited set of flow measurements, generally from an experiment, and a numerical simulation of the Navier–Stokes equations. The fluctuations are educed from resolvent analysis and time-resolved data at a single point in the flow. Resolvent analysis also guides where measurements of the mean and fluctuating quantities are needed for efficient reconstruction of a simple example case study: flow around a circular cylinder at a Reynolds number of  $Re = 100$ . For this flow, resolvent analysis reveals that the leading singular value, most amplified modes, and the mean profile for  $47 < Re < 320$  scale with the shedding frequency and length of the recirculation bubble. A relationship between these two parameters reinforces the notion that a wave maker, for which the length scales with the recirculation bubble, determines the frequency and region where an instability mechanism is active. The procedure offers a way to choose sensor locations that capture the main coherent structures of a flow and a method for computing mean pressure by using correctly weighted resolvent modes.

## Nomenclature

$a$	=	acceleration of vortex
$B$	=	mass matrix
$b$	=	half-velocity defect
$C$	=	operator mapping full state to velocity space
$C_{pb}$	=	base pressure coefficient
$D$	=	cylinder diameter
$\mathcal{E}$	=	discrepancy functional
$f$	=	mean momentum forcing
$f_s$	=	solenoidal component of mean momentum forcing
$g$	=	acceleration due to gravity
$\mathcal{H}$	=	resolvent operator
$L$	=	length of pendulum
$\mathcal{L}$	=	linear Navier–Stokes operator
$\mathcal{L}$	=	Lagrangian functional
$l_m$	=	recirculation bubble length
$M$	=	measurement subspace
$\mathcal{M}$	=	projection operator that maps numerical data to measurement subspace
$\bar{m}$	=	available measurements
$N$	=	number of points in the numerical domain
$p$	=	pressure

$R$	=	Reynolds stress tensor
$Re$	=	Reynolds number; $U_\infty D/\nu$
$St$	=	Strouhal number; $\omega D/U_\infty$
$U_c$	=	vortex convection velocity
$U_\infty$	=	inlet velocity
$\mathbf{u}$	=	velocity vector
$\mathcal{W}$	=	wave maker region
$w$	=	weight of a measurement point
$x_r$	=	location of the edge of the recirculation bubble
$\delta$	=	wavelength of resolvent mode
$\zeta$	=	absolute value of a quantity of interest (for example, the wave maker) for point weighting
$\lambda$	=	least stable eigenvalue of the linearized Navier–Stokes operator
$\nu$	=	kinematic viscosity
$\xi$	=	scalar potential for the irrotational component of $f$
$\sigma$	=	singular value of the resolvent operator
$\hat{\phi}$	=	right singular vector of $\mathcal{H}$ or resolvent forcing mode
$\chi$	=	complex amplitude of a resolvent mode; $\sigma\bar{\chi}$
$\bar{\chi}$	=	nonlinear weight of a resolvent mode
$\hat{\psi}$	=	left singular vector of $\mathcal{H}$ or resolvent response mode
$\omega$	=	temporal frequency

Received 6 September 2018; revision received 20 February 2019; accepted for publication 2 April 2019; published online 24 May 2019. Copyright © 2019 by the American Institute of Aeronautics and Astronautics, Inc. All rights reserved. All requests for copying and permission to reprint should be submitted to CCC at [www.copyright.com](http://www.copyright.com); employ the eISSN 1533-385X to initiate your request. See also AIAA Rights and Permissions [www.aiaa.org/randp](http://www.aiaa.org/randp).

\*Postdoctoral Research Fellow, University of Melbourne, Parkville, Victoria 3010, Australia. Member AIAA.

<sup>†</sup>Research Scientist, Fundamental and Experimental Aerodynamics Department, 8 rue des Vertugadins.

<sup>‡</sup>Professor, Department of Mathematics.

<sup>§</sup>Theodore von Kármán Professor of Aeronautics, Graduate Aerospace Laboratories, 1200 E. California Boulevard, MC 105-50. Associate Fellow AIAA.

## Subscripts

$A$	=	cost function depending on velocity
$B$	=	cost function depending on velocity and pressure
$b$	=	quantity at the base of the cylinder
$i$	=	initial value
$s$	=	shedding frequency
$t$	=	final value
$0$	=	base flow quantity

## Superscripts

$\dagger$	=	adjoint quantity
$*$	=	complex conjugate

## I. Introduction

A GROWING number of studies [1–7] has used the resolvent framework of McKeon and Sharma [8] to obtain approximate reconstructions of statistically stationary flows. The methodology requires two inputs: the mean velocity profile, and a single time-resolved probe. The mean profile is used as an input to resolvent analysis, which recasts the Navier–Stokes equations (NSEs) as a closed-loop system. The linear dynamics constitute a directional amplifier that is forced by the nonlinear interactions of velocity modes. A singular value decomposition of the resolvent operator reveals the dominant coherent structures, or modes, in the flow and their frequencies. The time-resolved probe is used to determine the amplitude and phase, or complex weight, of these modes; although, this may not be necessary for some flows, such as exact coherent states in Couette flow [9], which can be closed offline. The nature of the inputs makes this procedure appealing because the mean profile can be obtained without time-resolved measurements. It is also shown, in this paper, that only a sparse approximation of the mean profile is necessary, which reduces the number of measurements needed to glean a significant amount of information about the flow.

Figure 1 summarizes the flow reconstruction procedure, first developed by Gómez et al. [1] and Beneddine et al. [3], which will be expanded upon in this paper. As mentioned earlier, the mean profile and a single time-resolved probe are the necessary measurements. Because the mean may lack resolution or field of view requirements for resolvent analysis, we can employ data-assimilation [10], a technique whereby experimental measurements are merged with computational fluid dynamics [11], to fill in missing data. Data-assimilation can be traced back to meteorology [12] and has since been extended to the NSEs using a variational approach [13–15] where, similar to optimal control, the objective is to minimize a cost functional. The framework of Foures et al. [15] relied on non-time-resolved measurements from direct numerical simulation (DNS) to assimilate the mean flow around a circular cylinder using the Reynolds-averaged Navier–Stokes (RANS) equations. Symon et al. [16] developed it further for experimental data by implementing the algorithm for the mean flow around an idealized airfoil at a chord-based Reynolds number of  $Re_c = 13,500$ .

The second step in Fig. 1 is to data-assimilate the mean using the algorithm developed by Foures et al. [15]. Without mean pressure data, only the solenoidal component of the forcing to the mean momentum equations can be recovered. The irrotational component is lumped into the mean pressure gradient term, which prevents recovery of the mean pressure field. In this paper, the algorithm is extended to include pressure discrepancy measurements and determine where in the flow they have the greatest impact. Recent studies (e.g., Refs. [17–19]) have investigated optimal placement of sensors for flow reconstruction. One of the goals here is to identify the

domain where measurements are needed for successful data-assimilation of the mean flow. The quality of the reconstruction is assessed by comparing the mean forcings identified by the optimization to their counterparts from DNS. Flow around a circular cylinder at a Reynolds number of  $Re = 100$  is chosen to investigate measurements for data-assimilation. The results of Mantič-Lugo et al. [20] are the motivation for choosing a Reynolds number lower than Foures et al. [15], where  $Re = 150$ , because it is possible to obtain a self-consistent model that predicts the amplitude of the most unstable eigenmode in the flow. We draw connections between this approach and the effect of data-assimilation in Sec. IV.

The steady cylinder wake becomes unstable at a critical Reynolds number of  $Re = 47$  [21–23], resulting in the von Kármán vortex street. Step 3 in Fig. 1 is to perform a resolvent analysis on the mean wake which, as shown by Symon et al. [24], indicates that the globally most amplified mode occurs at the shedding frequency and captures the vortex street. This matches the results of Barkley [25], who determined that a stability analysis of the mean flow could identify the frequency of the vortex shedding, which becomes unstable to three-dimensional perturbations at  $Re = 189$  [26]. Leontini et al. [27] demonstrated that a global stability analysis of the span-averaged wake continues to identify the shedding frequency. Resolvent analysis thus assists in choosing and weighting measurement points because it identifies the scaling behavior of the resolvent and mean profile for  $60 < Re < 320$  and explains how the dominant amplifications are sustained by nonlinear interactions. Finally, it is demonstrated how the calibrated resolvent modes from step 4 can be used to approximate the mean pressure in step 5 without any a priori knowledge of the mean pressure field. Even though the input measurements for the reconstruction procedure are from simulation data, the methodology outlined in Fig. 1 can also be applied to experimental data (see Ref. [7]).

The rest of the paper is organized as follows. Section II describes the direct numerical simulations, the RANS simulations, the data-assimilation method, and the resolvent analysis of the mean flow. The framework of Foures et al. [15] is updated to include mean pressure measurements in addition to mean velocity measurements. In Sec. III, the DNS results are validated against well-known results in the literature. In Sec. IV, we compare data-assimilation of the mean flow using velocity-only measurements with data-assimilation using velocity and pressure measurements. In Sec. V, the scaling of the mean profile and most amplified resolvent mode help identify where experimental measurements are critical to the success of the data-assimilation. We also identify a link between the size of the wave maker, which scales with the mean recirculation length, to the shedding frequency. These results help guide how to truncate the measurement domain in Sec. VI without sacrificing the quality of mean flow reconstruction, and we conclude by commenting on application to higher-Reynolds-number flows in Sec. VII.

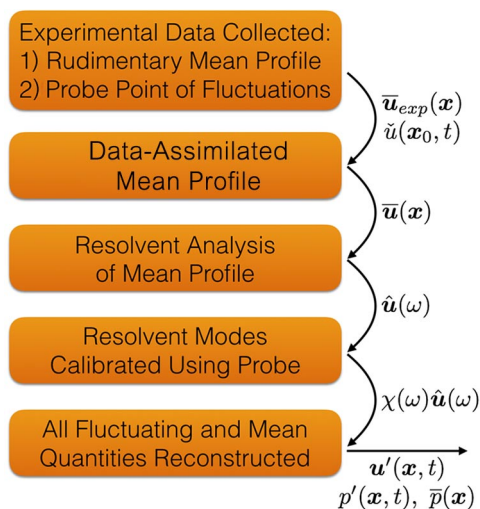


Fig. 1 Outline of the flow reconstruction procedure based on the works of Gómez et al. [1] and Beneddine et al. [3].

## II. Approach

### A. Direct Numerical Simulation

The flow around a circular cylinder is governed by the incompressible Navier–Stokes equations, which are nondimensionalized by the cylinder diameter  $D$  and inlet velocity  $U_\infty$ :

$$\partial_t \mathbf{u} + \mathbf{u} \cdot \nabla \mathbf{u} = -\nabla p + Re^{-1} \nabla^2 \mathbf{u} \quad (1a)$$

$$\nabla \cdot \mathbf{u} = 0 \quad (1b)$$

The states  $\mathbf{u}$  and  $p$  are the velocity and pressure, and  $Re$  is the Reynolds number based on  $D$  and  $U_\infty$ . Both two- and three-dimensional simulations are performed for  $60 < Re < 190$  and  $190 \leq Re \leq 320$ , respectively, because the flow becomes unstable to three-dimensional perturbations at  $Re = 189$  [26]. For all simulations, a uniform inlet velocity condition is prescribed. No-slip Dirichlet boundary conditions are applied to the cylinder surface,

symmetric conditions are applied to the upper and lower boundaries, and advective conditions are applied to the outlet.

The two-dimensional simulations are realized in FreeFem++ [28] using the same mesh and discretizations as those in Ref. [24]. The simulations are averaged in time over 25 vortex shedding cycles once the flow achieves a steady limit cycle state. Three-dimensional simulations are performed using the spectral-element/Fourier solver of Ref. [29] for  $190 \leq Re \leq 320$ . The code uses a spectral-element method for the spatial differencing in the cylinder plane and a Fourier decomposition for the spatial differencing in the spanwise direction. The domain has a blockage ratio of 4% with the upstream and side boundaries located  $12D$  from the center of the cylinder and the outflow positioned  $25D$  downstream of the cylinder. The spanwise extent is  $12D$ , and 48 Fourier planes are used. The mesh consists of 196 spectral elements and seventh-order Lagrangian interpolating polynomials. The flow is averaged in the spanwise direction once the flow has reached an asymptotic state. It is then averaged in time over about 60 shedding cycles because the flow is quasi periodic.

The mean profiles obtained from DNS are considered to be the ‘‘truth’’ to which we can compare the data-assimilation results. They are also the source of ‘‘limited’’ measurement points in Secs. IV and VI to the data-assimilation algorithm. How these points are chosen and which states should be measured (i.e., velocity and/or pressure) are discussed in Secs. IV–VI.

## B. RANS Simulation

The mean flow obeys the incompressible RANS equations:

$$\bar{\mathbf{u}} \cdot \nabla \bar{\mathbf{u}} + \nabla \bar{p} - Re^{-1} \nabla^2 \bar{\mathbf{u}} = \mathbf{f} \quad (2a)$$

$$\nabla \cdot \bar{\mathbf{u}} = 0 \quad (2b)$$

where an overbar denotes a time average, and  $\mathbf{f}$  can be written as

$$\mathbf{f} = -\nabla \cdot \mathbf{R}, \quad R_{ij} = \overline{u_i' u_j'} \quad (3)$$

The quantity  $\mathbf{R}$  is the Reynolds stress tensor, the divergence of which forces the mean momentum equations. The true  $\mathbf{f}$  is computed from the DNS snapshots. In the data-assimilation algorithm, only the mean velocity field is known a priori; so,  $\mathbf{f} = 0$  is used as an initial guess, and Eq. (2) is solved using a Newton–Raphson method [16].

## C. Data-Assimilation

The data-assimilation procedure begins by comparing a subset of DNS measurements to the prediction made by the RANS model. A Lagrangian functional  $\mathcal{L}$  penalizes the discrepancy between them and is used to derive the equations that determine how to iteratively update  $\mathbf{f}$  in order to minimize this discrepancy:

$$\begin{aligned} \mathcal{L}(\mathbf{f}, \bar{\mathbf{u}}, \bar{p}, \bar{\mathbf{u}}^\dagger, \bar{p}^\dagger) &= \mathcal{E}(\bar{\mathbf{u}}, \bar{p}) - \langle \bar{\mathbf{u}}^\dagger, \bar{\mathbf{u}} \cdot \nabla \bar{\mathbf{u}} + \nabla \bar{p} - Re^{-1} \nabla^2 \bar{\mathbf{u}} - \mathbf{f} \rangle \\ &\quad - \langle \bar{p}^\dagger, \nabla \cdot \bar{\mathbf{u}} \rangle \end{aligned} \quad (4)$$

where  $\langle \cdot, \cdot \rangle$  is the spatial scalar product

$$\langle \mathbf{a}, \mathbf{b} \rangle = \int_{\Omega} \mathbf{a} \cdot \mathbf{b} \, d\Omega \quad (5)$$

with  $\mathbf{a}$  and  $\mathbf{b}$  being functions of space. The first term on the right-hand side of Eq. (4) is the discrepancy between the measurements from the true mean field and the assimilated field. We modify the cost functional introduced in Ref. [15], which is here denoted as  $\mathcal{E}'_A$ , where

$$\mathcal{E}'_A(\bar{\mathbf{u}}) = \frac{1}{2} \|\bar{\mathbf{m}} - \mathcal{M}(\bar{\mathbf{u}})\|_M^2 \quad (6)$$

to include pressure via  $\mathcal{E}'_B$ :

$$\mathcal{E}'_B(\bar{\mathbf{u}}, \bar{p}) = \frac{1}{2} \|\bar{\mathbf{m}} - \mathcal{M}(\bar{\mathbf{u}}, \bar{p})\|_M^2 \quad (7)$$

The quantity  $\bar{\mathbf{m}}$  incorporates available measurements, and the operator  $\mathcal{M}$  projects the numerical data onto the measurement subspace  $M$ . The final values of the cost functional, denoted by the superscript  $t$ , are further normalized by their initial values, denoted by the superscript  $i$ , such that

$$\mathcal{E}_A(\bar{\mathbf{u}}) = \mathcal{E}'_A^t / \mathcal{E}'_A^i \quad (8)$$

$$\mathcal{E}_B(\bar{\mathbf{u}}, \bar{p}) = \mathcal{E}'_B^t / \mathcal{E}'_B^i \quad (9)$$

To minimize  $\mathcal{L}$ , the first variations with respect to each dependent variable are set to zero. The first variation with respect to the adjoint state variables yields the incompressible RANS equations, which are constraints to the optimization problem. The first variation with respect to  $\mathbf{f}$  reveals how to update the forcing:

$$\nabla_f \mathcal{E} = \bar{\mathbf{u}}^\dagger \quad (10)$$

Finally, the adjoint RANS equations are derived by obtaining the first variation with respect to the forward state variables:

$$-\bar{\mathbf{u}} \cdot \nabla \bar{\mathbf{u}}^\dagger + \bar{\mathbf{u}}^\dagger \cdot \nabla \bar{\mathbf{u}}^T - \nabla \bar{p}^\dagger - Re^{-1} \nabla^2 \bar{\mathbf{u}}^\dagger = \frac{\delta \mathcal{E}}{\delta \bar{\mathbf{u}}} \quad (11a)$$

$$\nabla \cdot \bar{\mathbf{u}}^\dagger = \frac{\delta \mathcal{E}}{\delta \bar{p}} \quad (11b)$$

The forcing term on the right-hand side of Eq. (11b) is the only term that is different from Foures et al. [15], where the adjoint velocity is constrained to be divergence free. The reconstructed forcing is consequently not limited to the solenoidal component. Performing a Helmholtz decomposition on  $\mathbf{f}$  yields the following:

$$\mathbf{f} = \nabla \xi + \mathbf{f}_s \quad (12)$$

where  $\nabla \xi$  represents the divergence or irrotational component, and  $\mathbf{f}_s$  is the solenoidal or rotational component. When only  $\mathbf{f}_s$  is recovered, the rotational part  $\nabla \xi$  is lumped in with the mean pressure term in the RANS equations:

$$\bar{\mathbf{u}} \cdot \nabla \bar{\mathbf{u}} + \nabla(\bar{p} - \xi) + Re^{-1} \nabla^2 \bar{\mathbf{u}} = \mathbf{f}_s \quad (13)$$

The full  $\mathbf{f}$ , which appears in Eq. (2a), can be retained by incorporating pressure measurements into the data-assimilation algorithm.

Table 1 summarizes the various cases that are considered in the study. In Sec. IV, we discuss cases 1A and 1B, where measurements are known in the full domain of the DNS. In Sec. VI, the optimal placement of velocity and pressure measurements is assessed. Cases 2A–6B limit the measurement domain, which implies that the forcing to the adjoint RANS equations is zero where the flow is not measured. Finally, the measurement points are weighted to stress the underlying physics of the flow in cases 7–9 to assess whether this affects the algorithm’s performance. Measurements may also be weighted less if they are more susceptible to noise contamination, for example. The weight for any point is given by the following:

$$w = 1 + 2 \frac{\zeta}{\max(\zeta)} \quad (14)$$

where  $\zeta$  is the absolute value of some quantity of interest such as the wave maker (see Sec. V). Points far away from these regions are therefore still assigned a weight of at least unity. The multiplicative

**Table 1** Domains, numbers and weightings of points, assimilated states, final normalized cost functionals, and least stable eigenvalues of the various cases studied

Case	Domain	$N$	Weighting	States	$\mathcal{E}_A$ %	$\mathcal{E}_B$ %	$\lambda$
1A	Full	313,048	None	$\bar{\mathbf{u}}$	2.14e-5	—	1.81e-3 + 1.02i
1B	Full	365,358	None	$\bar{\mathbf{u}}, \bar{p}$	—	3.77e-5	1.76e-3 + 1.02i
2A	$x \in [-2,6] \cup y \in [-2,2]$	16,780	None	$\bar{\mathbf{u}}$	3.29	—	1.83e-3 + 1.02i
2B	$x \in [-2,6] \cup y \in [-2,2]$	19,591	None	$\bar{\mathbf{u}}, \bar{p}$	—	4.54	1.28e-3 + 1.02i
3A	$x \in [-1,3] \cup y \in [-2,2]$	9,502	None	$\bar{\mathbf{u}}$	5.05	—	1.83e-3 + 1.02i
3B	$x \in [-1,3] \cup y \in [-2,2]$	11,102	None	$\bar{\mathbf{u}}, \bar{p}$	—	6.56	1.63e-3 + 1.02i
4A	$x \in [-1,2] \cup y \in [-2,2]$	5,176	None	$\bar{\mathbf{u}}$	9.73	—	1.31e-2 + 1.01i
4B	$x \in [-1,2] \cup y \in [-2,2]$	6,053	None	$\bar{\mathbf{u}}, \bar{p}$	—	10.6	1.08e-2 + 1.01i
5A	$x \in [1,3] \cup y \in [-2,2]$	4,976	None	$\bar{\mathbf{u}}$	5.31	—	3.52e-3 + 1.02i
5B	$x \in [1,3] \cup y \in [-2,2]$	5,815	None	$\bar{\mathbf{u}}, \bar{p}$	—	6.9	1.71e-3 + 1.02i
6A	$x \in [2,4] \cup y \in [-2,2]$	4,902	None	$\bar{\mathbf{u}}$	5.31	—	1.84e-3 + 1.02i
6B	$x \in [2,4] \cup y \in [-2,2]$	5,722	None	$\bar{\mathbf{u}}, \bar{p}$	—	6.4	1.29e-3 + 1.02i
7	Full	313,048	Wave maker	$\bar{\mathbf{u}}$	1.79e-5	—	1.76e-3 + 1.02i
8	Full	313,048	Response mode	$\bar{\mathbf{u}}$	1.83e-5	—	1.77e-3 + 1.02i
9	Full	313,048	Iterative	$\bar{\mathbf{u}}$	2.11e-5	—	1.75e-3 + 1.02i

factor of two in Eq. (14) is a compromise between emphasizing important flow physics without drowning out the contributions from other regions in the domain. A factor of five, for example, leads to poorer convergence, whereas a factor of one mitigates the benefit of weighting.

### D. Resolvent Analysis

The resolvent operator is derived by Reynolds decomposing the velocity field of Eq. (1) into a mean and fluctuating component (denoted by a prime)  $\mathbf{u} = \bar{\mathbf{u}} + \mathbf{u}'$ . Time averaging this equation results in Eq. (2) that, when subtracted from Eq. (1), yields the equations for the fluctuations:

$$\begin{aligned} \partial_t \mathbf{u}' + \bar{\mathbf{u}} \cdot \nabla \mathbf{u}' + \mathbf{u}' \cdot \nabla \bar{\mathbf{u}} + \nabla p' - Re^{-1} \nabla^2 \mathbf{u}' \\ = -\mathbf{u}' \cdot \nabla \mathbf{u}' + \overline{\mathbf{u}' \cdot \nabla \mathbf{u}'} \end{aligned} \quad (15a)$$

$$\nabla \cdot \mathbf{u}' = 0 \quad (15b)$$

Setting  $-\mathbf{u}' \cdot \nabla \mathbf{u}' + \overline{\mathbf{u}' \cdot \nabla \mathbf{u}'} = \mathbf{f}'$  and treating  $\mathbf{f}'$  as an unknown harmonic forcing  $\mathbf{f}' = \hat{\mathbf{f}} e^{i\omega t}$  implies that the velocity response will also be harmonic (i.e.,  $\mathbf{u}' = \hat{\mathbf{u}} e^{i\omega t}$ ) due to linearity. Substituting these forms into Eq. (15a) and rearranging terms yields the following:

$$\hat{\mathbf{u}} = \mathbf{C}^T (i\omega \mathbf{B} - \mathbf{L})^{-1} \mathbf{C} \hat{\mathbf{f}} = \mathcal{H}(\omega) \hat{\mathbf{f}} \quad (16)$$

where  $\mathcal{H}(\omega)$  is the resolvent operator,  $\mathbf{C} = (10)^T$ , and  $\mathbf{B} = \mathbf{C}\mathbf{C}^T$ . The operator  $\mathbf{C}$  converts between the velocity subspace (there are no terms that are nonlinear with respect to pressure) to the full-state space. The numerical discretization of matrix  $\mathbf{A} = i\omega \mathbf{B} - \mathbf{L}$  is sparse, and the linear Navier–Stokes (LNS) operator  $\mathbf{L}$  has the following form:

$$\mathbf{L} = \begin{pmatrix} -\bar{\mathbf{u}} \cdot \nabla() - () \cdot \nabla \bar{\mathbf{u}} + Re^{-1} \nabla^2() & -\nabla() \\ \nabla \cdot () & 0 \end{pmatrix} \quad (17)$$

The linear operators for resolvent analysis are formed in FreeFem+ using P2 and P1 Taylor–Hood finite elements for velocity and pressure, respectively. The equations are recast into weak form, and the singular values are computed by reformulating the singular value decomposition as an eigenvalue problem:

$$\mathcal{H}^*(\omega) \mathcal{H}(\omega) \hat{\boldsymbol{\phi}}_j = \sigma_j^2 \hat{\boldsymbol{\phi}}_j \quad (18)$$

where  $\hat{\boldsymbol{\phi}}_j$  is the  $j$ th singular vector, or resolvent forcing mode, with an associated gain of  $\sigma_j$ . The resolvent response modes  $\hat{\boldsymbol{\psi}}_j$  can be computed by finding the largest eigenvalues of  $\mathcal{H}^*(\omega) \mathcal{H}(\omega)$  (see Ref. [30] for details) such that

$$\mathcal{H}(\omega) = \sum_{j=1}^{\infty} \hat{\boldsymbol{\psi}}_j \sigma_j \hat{\boldsymbol{\phi}}_j^* \quad (19)$$

The method solves for the largest eigenvalues of  $\mathcal{H}^*(\omega) \mathcal{H}(\omega)$  using a Krylov method to extract the eigenvalues of largest magnitude. In the present case, the Arnoldi Package library [31] is used and the matrix inverses of  $\mathcal{H}(\omega)$  and  $\mathcal{H}^*(\omega)$  are obtained using a direct sparse lower–upper solver with the MULTifrontal MASSively Parallel sparse direct Solver library [32]. Because finite elements are used, the Jacobian matrices are sparse and can be computed explicitly. The choice of  $\omega$  is arbitrary; although, for the flows considered in this study, the frequency where the resolvent norm, or largest singular value  $\sigma_1$ , peaks corresponds to the least stable eigenvalue of the LNS operator and can be computed from an eigenanalysis (see Ref. [24]). The most amplified resolvent response modes give insight into the dominant physical mechanisms of the flow. Their structure, therefore, is likely to identify locations where the fluctuations are strong and lead to the formation of Reynolds stresses; this guides the choice of domain and point weighting in Sec. VI.

### E. Weight Calibration

The weight of a response mode is determined by computing the projection of the nonlinear forcing onto the resolvent forcing mode:

$$\hat{\mathbf{u}}(\omega) = \sum_j \hat{\boldsymbol{\psi}}_j(\omega) \sigma_j(\omega) (\hat{\mathbf{f}}(\omega) \cdot \hat{\boldsymbol{\phi}}_j(\omega)) = \sum_j \hat{\boldsymbol{\psi}}_j(\omega) \sigma_j(\omega) \bar{\chi}_j(\omega) \quad (20)$$

where  $\bar{\chi}_j(\omega)$  is the weight associated with the  $j$ th response mode [33]. Because the first singular value is much larger than the second one for cylinder flow (see Ref. [24]), the weights of the first resolvent response modes ( $j = 1$ ) are computed without knowledge of the nonlinear term. Instead, we follow Refs. [1,3], where time-resolved knowledge of the velocity fluctuations at a single point  $\mathbf{x}_0$  is used to determine the complex amplitude  $\chi_1$ , which is defined as

$$\chi_1(\omega) = \sigma_1(\omega) \bar{\chi}_1(\omega) \quad (21)$$

The final expression for the velocity fluctuations at a given frequency is

$$\hat{\mathbf{u}}(\omega) \approx \chi_1(\omega) \hat{\boldsymbol{\psi}}_1(\omega) \quad (22)$$

Equation (22) can be applicable to more complex flows (e.g., Ref. [3]) but is not for frequencies where  $\sigma_1 \approx \sigma_2$  because multiple modes are required to reconstruct the fluctuations. Because the resolvent operator tends to be low rank at energetic frequencies (e.g., Ref. [34]), we discard frequencies where this is not the case.

The vertical velocity  $v$  is chosen over the streamwise velocity  $u$  because the former can more easily identify the frequency content of

this flow (this choice is likely to be flow specific). The signal is Fourier transformed in time, yielding  $\hat{v}(\omega, \mathbf{x}_0)$ . This complex-valued function of  $\omega$  predicts the amplitude of the corresponding resolvent mode through the following expression:

$$\chi_1(\omega) = \hat{v}(\omega, \mathbf{x}_0) / \tilde{v}(\omega, \mathbf{x}_0) \quad (23)$$

where  $\hat{v}(\omega, \mathbf{x}_0)$  is the value of the unscaled resolvent response mode at  $\mathbf{x}_0$ . The reader is referred to the works of Towne et al. [6], Rosenberg [9], and McKeon et al. [33] for other ways to obtain the amplitudes.

#### F. Mean Pressure Correction

The correctly weighted resolvent response modes can be used to correct the mean pressure when velocity-only measurements are available. The forcing to the mean momentum equation is rewritten as a sum of resolvent modes:

$$\begin{aligned} \bar{\mathbf{u}} \cdot \nabla \bar{\mathbf{u}} + \nabla \bar{p} - Re^{-1} \nabla^2 \bar{\mathbf{u}} = & - \sum_{\omega} \sum_{j=1}^N 2 \text{Real}(\chi_j(\omega) \hat{\boldsymbol{\psi}}_j(\omega) \\ & \cdot \chi_j(-\omega) \nabla \hat{\boldsymbol{\psi}}_j(-\omega)) \end{aligned} \quad (24)$$

where  $\chi_j$  is the amplitude of the  $j$ th resolvent response mode determined using the procedure mentioned earlier. The right-hand side of Eq. (24) is a sum of triadic interactions where a mode with frequency  $\omega$  interacts with its conjugate at frequency  $-\omega$  to produce the Reynolds stresses required to sustain the mean profile. The right-hand side of Eq. (24) consists of both rotational and irrotational components, unlike the velocity-only data-assimilated forcing, which is divergence free.

Combining Eqs. (12), (13), and (24) yields an equation for  $\xi$ :

$$\nabla \xi = - \sum_{\omega} \sum_{j=1}^N 2 \text{Real}(\chi_j(\omega) \hat{\boldsymbol{\psi}}_j(\omega) \cdot \chi_j(-\omega) \nabla \hat{\boldsymbol{\psi}}_j(-\omega)) - \mathbf{f}_s \quad (25)$$

Taking the divergence of Eq. (25), one eliminates  $\mathbf{f}_s$  and obtains a Poisson equation for  $\xi$ :

$$\nabla^2 \xi = - \nabla \cdot \left[ \sum_{\omega} \sum_{j=1}^N 2 \text{Real}(\chi_j(\omega) \hat{\boldsymbol{\psi}}_j(\omega) \cdot \chi_j(-\omega) \nabla \hat{\boldsymbol{\psi}}_j(-\omega)) \right] \quad (26)$$

By recalling that  $\mathbf{f} = -\overline{\mathbf{u}' \cdot \nabla \mathbf{u}'}$ , it can be noted that  $\mathbf{f}$  should be zero at the wall and at infinity. By taking the divergence of Eq. (12), one obtains

$$\nabla \cdot \mathbf{f} = \nabla^2 \xi \quad (27)$$

In principle, setting  $\mathbf{f}_s = 0$  at the wall would also imply that  $\nabla \xi = 0$  at the wall. Because this boundary condition is not compatible with the Laplace equation, the Neumann boundary condition  $\partial \xi / \partial n = 0$  is chosen in partial fulfillment of no slip at the boundary. In the far field, both  $\mathbf{f}$  and  $\mathbf{f}_s$  approach zero, and thus  $\nabla \xi \rightarrow 0$  to ensure that  $\xi \rightarrow 0$ . The true pressure field can be recovered by

$$\bar{p} = \xi + \tilde{p} \quad (28)$$

where  $\tilde{p}$  is the pressure determined by data-assimilation, based solely on velocity measurements. This is true because it is assumed  $\mathbf{f}_s$  is approximately equal to the solenoidal forcing stemming from the data-assimilation procedure (which is not exactly true due to the mismatch of the boundary condition at the wall; i.e., no slip is not equivalent to slip).

### III. Validation of DNS Results

In this section, we validate the DNS with respect to the literature and present results that form the truth for the reconstructions that

follow. The shedding frequency  $\omega_s$  has been plotted in Fig. 2 alongside experimental results from Ref. [35]. The agreement in the two-dimensional regime ( $Re < 190$ ) is excellent, although there are minor discrepancies in the three-dimensional regime. The simulations successfully distinguish between the two modes that characterize the three-dimensional transition of the flow [36]. Mode A results in a discontinuous drop of the shedding frequency for  $190 \leq Re < 230$  before it reverts back to larger values when mode B takes over for  $Re \geq 240$ . The globally most amplified frequency identified by the resolvent is also plotted in Fig. 2, and it agrees well with the shedding frequency measured directly from the DNS.

To validate the pressure field, we compute the base pressure coefficient  $C_{pb}$  given by

$$C_{pb} = -2 \left( \frac{p_b - p_{\infty}}{\rho U^2} \right) \quad (29)$$

where  $p_b$  is the time-averaged pressure at the base of the cylinder, or  $\mathbf{x} = (0.5, 0)$ . The results are presented in Fig. 3 and are compared to the experimental results of Williamson and Roshko [37] and the simulations of Henderson [38]. Good agreement is observed for the base flow and Reynolds numbers below 260, whereas the DNS underpredicts  $C_{pb}$  for the highest Reynolds numbers considered.

Finally, the mean profile and second-order statistics for  $Re = 150$  are presented in Fig. 4 because the results can be compared directly to those of Foures et al. [15]. Figure 4a shows contours of the mean streamwise velocity  $\bar{u}$ , including the  $\bar{u} = 0$  contour in green. The length of the recirculation zone agrees with the results of Leontini

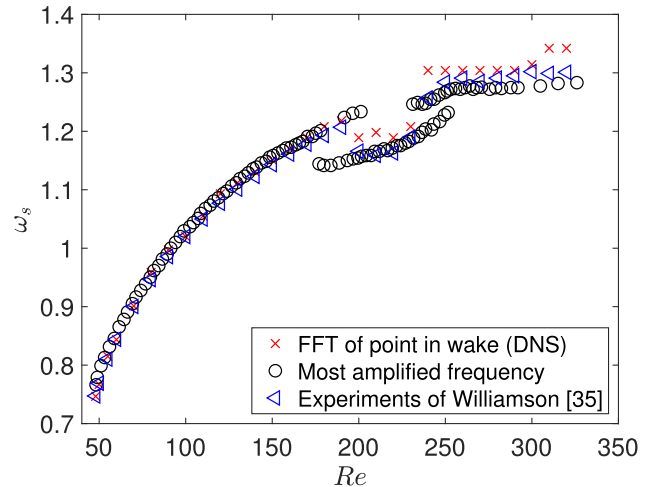


Fig. 2 Shedding frequency  $\omega_s$  as a function of Reynolds number  $Re$  Fast Fourier transform (FFT).

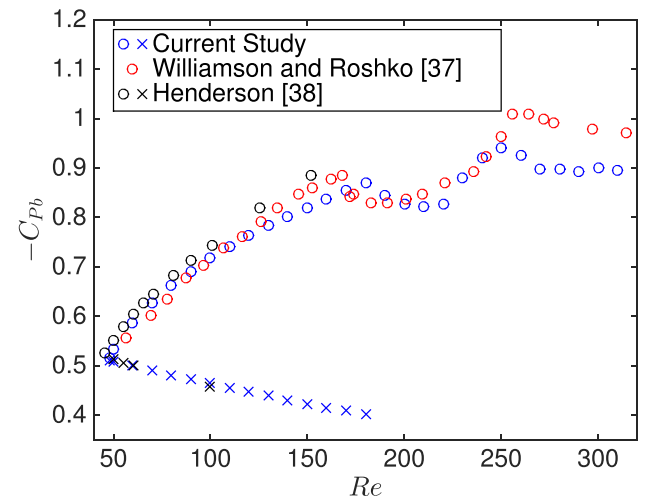


Fig. 3 Base pressure coefficient  $C_{pb}$  as a function of Reynolds number  $Re$  for the mean flow (circles) and the base flow (crosses).

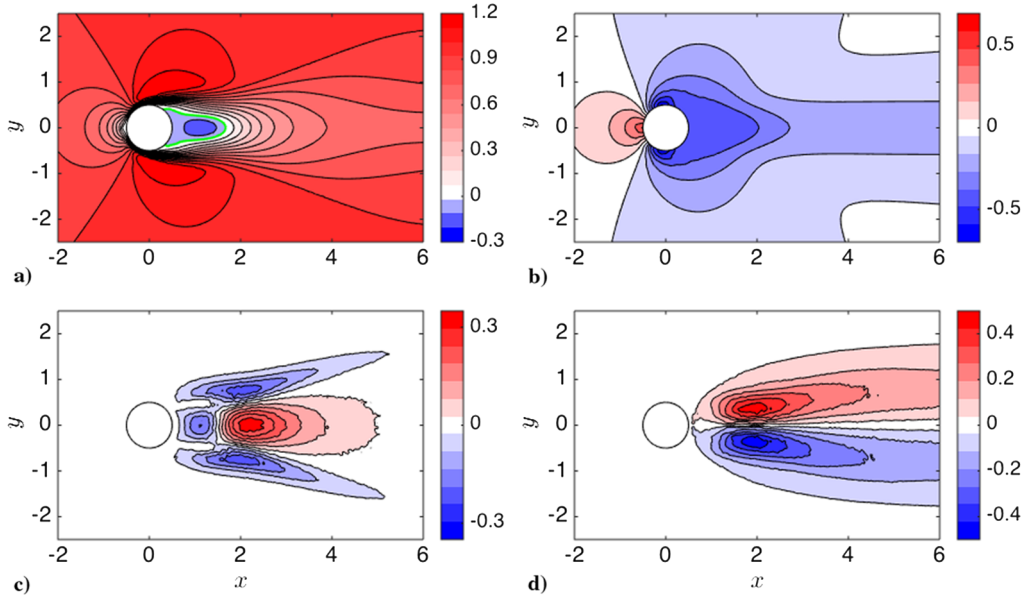


Fig. 4 2-D DNS results for  $Re = 150$ : a)  $\bar{u}$ , b)  $\bar{p}$ , c)  $f_x$ , and d)  $f_y$ .

et al. [27]. The mean pressure  $\bar{p}$  is plotted in Fig. 4b and agrees with the mean pressure field in the work of Foures et al. [15]. The  $x$  and  $y$  components of the (true) mean forcing  $f$  [Eq. (3)] are plotted in Figs. 4c and 4d, respectively. They also match with their counterparts in the work of Foures et al. [15].

#### IV. Data-Assimilation Results for Full Domain

##### A. Comparing Cases with and without Pressure Measurements

Having validated the DNS results with respect to the literature, we fix the Reynolds number to be  $Re = 100$  and consider cases where the mean states are known in the whole DNS domain. The first two cases assume knowledge of the velocity field everywhere in the domain and full-state knowledge of velocity and pressure everywhere in the domain. These are denoted as cases 1A and 1B (see Table 1), respectively, where cost functional A [or Eq. (8)] corresponds to case 1A, and cost functional B [or Eq. (9)] corresponds to case 1B. Even though the domains are truncated for some cases,  $\mathcal{E}_A$  and  $\mathcal{E}_B$  will be used to make fair comparisons among all the cases. The cost functional declines to  $\mathcal{E}_A = 2.14 \times 10^{-7}$ , as seen in Fig. 5, which is similar to the optimization performed by Foures et al. [15]. Excellent agreement is obtained between the data-assimilated mean velocity profile for case 1A/1B and the DNS as seen in Figs. 6a–6c. Cost functional A is also plotted in Fig. 5 for case 1B, and it is noticeably slower because it is also trying to assimilate pressure measurements.

Case 1B is able to reconstruct the mean pressure and its cost functional, which includes the mean pressure discrepancies, declines to  $\mathcal{E}_B = 3.77 \times 10^{-7}$ . Figures 6d–6f compare the mean pressures for case 1A, case 1B, and the DNS. As expected, case 1B is almost an identical match with the DNS because it is given the mean pressure information in the whole domain. Case 1A, on the other hand, does well in most regions of the flow, with the exception of the wake behind the recirculation zone from  $2 \leq x \leq 4$ . It is encouraging that it does this well without any knowledge of the mean pressure field.

Figure 6 also presents the  $x$  and  $y$  components of the mean forcing  $f$  in Figs. 6g–6i and 6j–6l, respectively. Case 1B exactly reconstructs both components of the mean forcing, as it should, because the adjoint velocity field is not constrained to be divergence free. Case 1A, on the other hand, is limited to capturing only the solenoidal component of the mean forcing. The agreement between  $f_x$  for case 1A in Fig. 6g and case 1B in Fig. 6h, nevertheless, is remarkably good; although, there are small differences between them, such as the location along the centerline of the peak mean forcing and the small lobe of negative mean forcing immediately behind the cylinder, which does not appear in case 1A. Notably,  $f_y$  is virtually zero

everywhere for case 1A, as seen in Fig. 6j when compared to case 1B in Fig. 6k.

##### B. Implications for Experimental Data

The full domain results suggest that the irrotational component of the forcing for this two-dimensional (2-D) flow is primarily in the  $y$  direction, whereas the solenoidal component is primarily in  $x$ . Such an observation can be explained by considering a simple case: parallel viscous flow in a channel where  $\bar{u} = \bar{u}(y)$ . Due to homogeneity in the  $x$  and  $z$  directions and no slip at the wall, the RANS equations become the following:

$$\partial_x \bar{p} - Re^{-1} \partial_{yy} \bar{u} = -\partial_y \overline{u'v'} \quad (30a)$$

$$\partial_y \bar{p} = -\partial_y \overline{v'v'} \quad (30b)$$

The mean forcing, therefore, is

$$\mathbf{f} = \begin{pmatrix} f_x \\ f_y \\ f_z \end{pmatrix} = \begin{pmatrix} -\partial_y \overline{u'v'} \\ -\partial_y \overline{v'v'} \\ 0 \end{pmatrix} \quad (31)$$

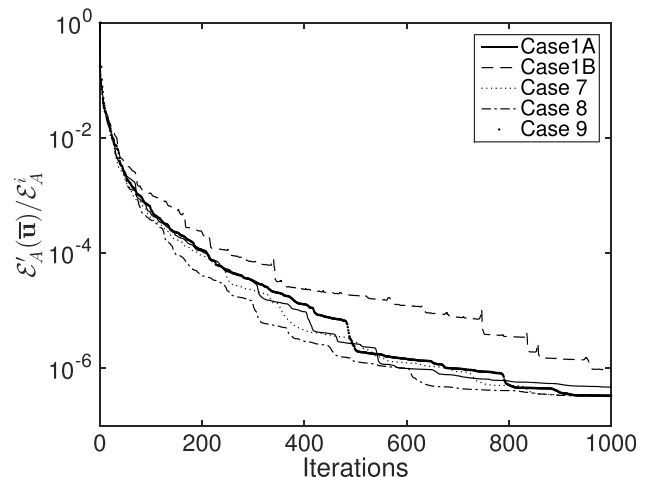


Fig. 5 Cost functional  $\mathcal{E}'_A(\bar{u})/\mathcal{E}_A^i$  plotted for various cases. Only the first 1000 iterations have been shown for clarity.

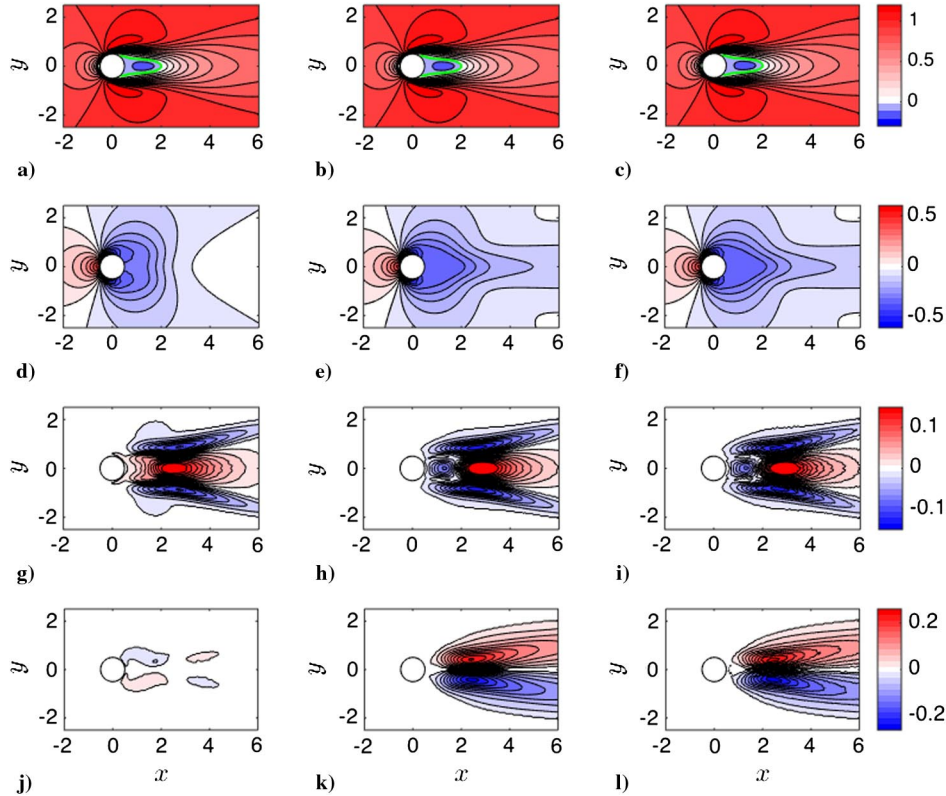


Fig. 6 Top to bottom:  $\bar{u}$ ,  $\bar{p}$ ,  $f_x$ , and  $f_y$  for cases 1A (left column), 1B (center column), and DNS (right column).

The divergence of  $\mathbf{f} = \nabla \xi + \mathbf{f}_s$  eliminates  $\mathbf{f}_s$  and can be equated to the divergence of Eq. (30):

$$\partial_{yy} \xi = -\partial_y \overline{v'v'} \quad (32)$$

Integrating Eq. (32) with respect to  $y$  results in

$$\nabla \xi = -\partial_y \overline{v'v'} = f_y \quad (33)$$

because  $y$  is the only nonhomogeneous direction in the flow and  $\partial_y \overline{v'v'}$  is zero at the walls. Thus, for a parallel viscous flow,  $\nabla \xi = f_y$  and  $\mathbf{f}_s = f_x$ .

The mean flow around the cylinder is not parallel, although the transverse velocity component is outweighed by the streamwise component in most regions of the flow. The only portions of the flow where this is not true are the front half of the cylinder, where the fluid is diverted around the body, and the wake immediately behind the cylinder, where there is a mismatch in  $f_x$  between cases 1A and 1B. In general, as long as the flow is weakly nonparallel,  $f_x$  is accurately captured by the data-assimilation algorithm using velocity-only measurements. In experimental settings where the mean pressure is not measured, one could compare  $f_x$  computed from the experiment with its data-assimilation counterpart and expect a reasonable match, assuming the flow is weakly nonparallel; e.g., Ref. [7]. It would not be necessary to compare the curl of the forcing (i.e.,  $\nabla \times \mathbf{f}$ ), as was done by Symon et al. [16], which requires computing two gradients of the Reynolds stress fields in order to assess the degree of success of the assimilation.

### C. Stabilizing Feedback

The data-assimilation algorithm can be interpreted as a controller that determines the feedback, in this case,  $\mathbf{f}$ , which stabilizes the mean profile. A linear stability analysis of the base flow reveals a pair of unstable eigenvalues where  $\lambda = 0.118 \pm 0.749i$  for  $Re = 100$ . A stability analysis of the mean profile is performed over various iterations of the optimization procedure for case 1A. The real and imaginary components of the least stable eigenvalue are plotted in Fig. 7. Iteration 0.1 corresponds to the eigenvalue of the base flow, or

the case where  $\mathbf{f} = 0$ . As the number of iterations increases, the growth rate declines until it reaches zero; whereas the imaginary part increases until it reaches the frequency of the saturated vortex shedding. These results are reminiscent of Mantič-Lugo et al. [20], who constructed a self-consistent model of the mean cylinder wake by adjusting the amplitude of the vortex shedding mode until the mean profile was marginally stable. They modeled  $\mathbf{f}$  using  $2\text{Real}(\tilde{\mathbf{u}}_1 \cdot \tilde{\mathbf{u}}_1^*)$ , where  $\tilde{\mathbf{u}}_1$  is the vortex shedding mode. In this approach, we do not assume that  $\mathbf{f}$  arises due to a single frequency, but the validity of approximating it from a single mode can be useful, as will be discussed in Sec. VI.

As an additional measure of whether the reconstructed mean velocity field is accurate, the least stable eigenvalue  $\lambda$  is reported in Table 1. A poorly data-assimilated field does not identify the correct value of  $\lambda = 0 + 1.02i$ . For the cases discussed in this section,  $\lambda$  is very accurately predicted, which is to be expected because the algorithm has knowledge of the velocity everywhere in the domain. The objectives of the next section are to understand how the scaling of

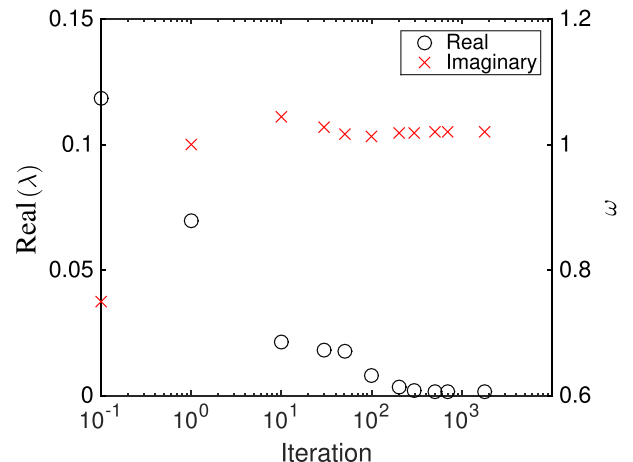


Fig. 7 Assimilated flow's least stable eigenvalue  $\lambda$  at various iterations. Iteration  $10^{-1}$  corresponds to the initial eigenvalue, or iteration zero.

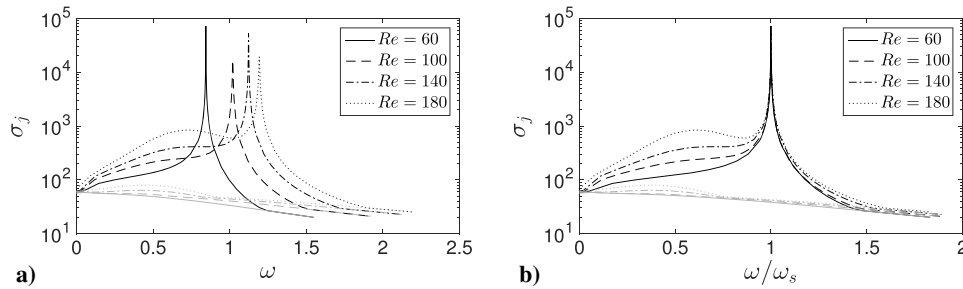


Fig. 8 First singular value  $\sigma_1$  (black) and second singular value  $\sigma_2$  (gray): a) plotted versus  $\omega$ , and b)  $\omega$  normalized by  $\omega_s$ .

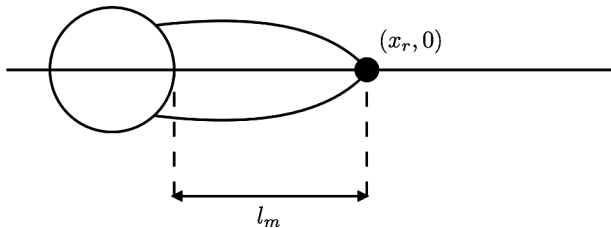


Fig. 9 Schematic of the cylinder recirculation bubble.

the mean profile is related to the frequency of the amplified coherent structures and to exploit features of the flow physics to provide rationale for the truncation of measurements.

## V. Resolvent Analysis and Scaling Behavior

### A. Scaling of the Resolvent Norm and Mean Profile

For this flow and Reynolds number range, the characteristics of the resolvent itself give insight into the underlying scaling of the mean profile and most amplified modes. It was noted in Sec. II that the resolvent norm peaks at the temporal frequency corresponding to the imaginary part of the least stable eigenvalue. As noted in Ref. [39], when the real part of the eigenvalue approaches the imaginary axis, the resolvent operator becomes singular, hence a large peak in the resolvent norm. For the mean wake around a circular cylinder, the peak occurs at the shedding frequency  $\omega_s$  as seen in Fig. 8a, where the leading singular values for several Reynolds numbers have been plotted. The location of the peak in the resolvent norm collapses in Fig. 8b when the frequency axis is scaled by  $\omega_s$ . A scaling for the peak resolvent norm as a function of the Reynolds number could not be determined because the real part of the eigenvalue is nearly zero;

consequently, the resolvent norm is sensitive to the spatial resolution and temporal convergence of the mean flow.

By consideration of the mean profile, it can be shown that  $\bar{u}(x, y)$  scales with  $St = \omega_s D / U_\infty$  at the recirculation point  $x_r$ , or the streamwise location where the mean flow along the centerline switches direction from negative to positive, implying  $\bar{u}(x = x_r, y = 0) = 0$ . In this study,  $l_m$  is the recirculation length and is defined as the distance from the edge of the cylinder to the recirculation point (see schematic in Fig. 9). The mean streamwise velocity profiles for the Reynolds numbers considered earlier are plotted in Figs. 10a and 10b and collapse almost perfectly when  $y$  is scaled by the Strouhal number  $St$ . The mean profiles for a square cylinder and the three-dimensional cylinder wake were also studied to see whether or not the same scaling applied. The results are plotted in Figs. 11a and 11b and follow the same trends as the two-dimensional cylinder wake. Similar scaling of the location of the peak resolvent norm is observed for these flows as for the two-dimensional circular cylinder wake in Fig. 8, underscoring the importance of the similarity characteristics of the mean flow.

### B. Scaling of the Dominant Resolvent Modes

The signature of  $\omega_s$  can also be observed in the optimal resolvent forcing and response modes. The scaling of the former is simpler and is addressed first. The amplitude of the forcing modes along the centerline of the domain for  $Re = 60$  and  $Re = 180$  is plotted in Fig. 12a. The spatial support is limited to upstream of the cylinder as well as the region immediately behind it. A convection velocity can be computed using  $U_c = \delta \omega_s / 2\pi$ , where  $\delta$  is the spatial wavelength of the forcing mode in Fig. 12a sufficiently upstream of the cylinder, where it is constant; i.e., it does not depend on  $x$ . For  $Re = 60$ ,  $\delta = 7.44$  and  $\omega_s = 0.844$ , yielding a convection velocity of  $U_c = 1$ . In fact, the convection velocity for all Reynolds numbers is equal to

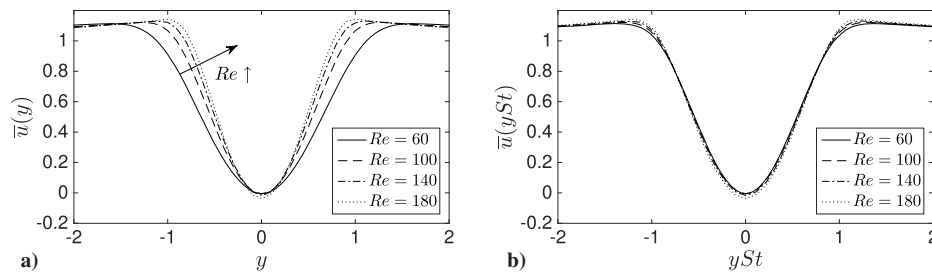


Fig. 10 Mean profiles  $\bar{u}(y)$  at the recirculation point  $x = x_r$ . The  $y$  axis is rescaled by the Strouhal number  $St$  in Fig. 10b.

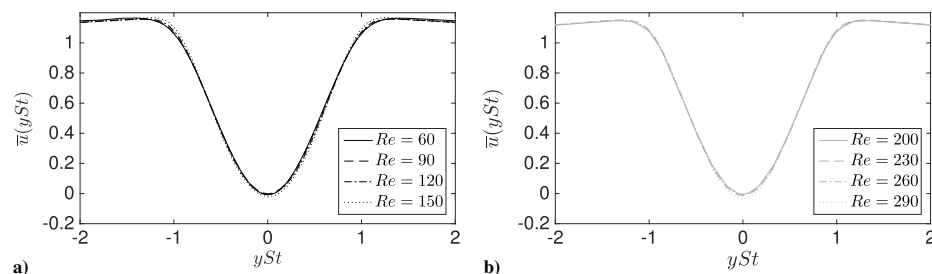
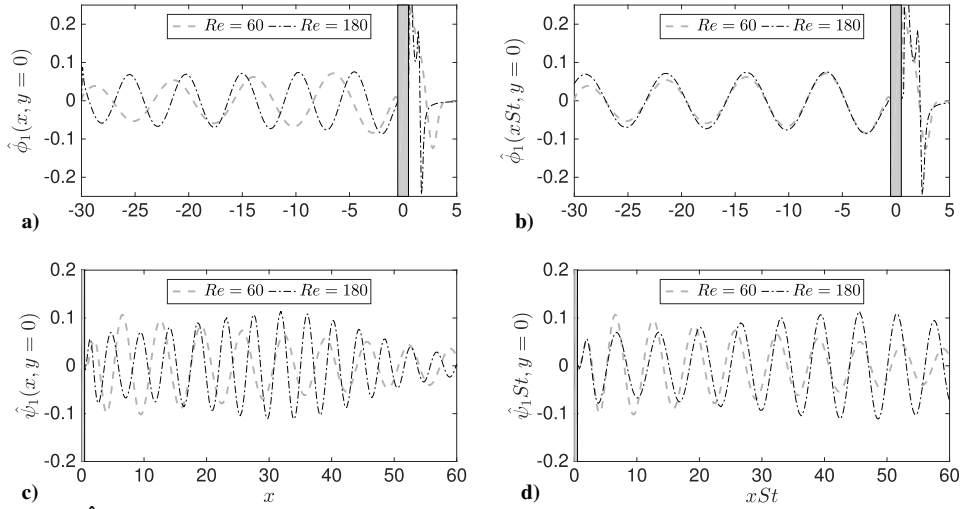


Fig. 11 Rescaled mean profiles  $\bar{u}(y)$  at the recirculation point for the a) square cylinder and b) three-dimensional cylinder wake.



**Fig. 12** Representations of a)  $\hat{\phi}_1(\omega_s)$  and c)  $\hat{\psi}_1(\omega_s)$  along the centerline  $y = 0$ . The modes are rescaled by the Strouhal number  $St$  in Figs. 12b and 12d.

unity for the forcing mode sufficiently upstream of the cylinder, and this is compatible with the fact that  $\bar{u}(x, y=0) = 1$  in this region. Consequently, an adjoint perturbation is transported at a convection velocity equal to the local mean velocity. The forcing modes along the centerline, where the mean velocity is unity upstream of the cylinder, collapse when scaled by the Strouhal number  $St$  in the streamwise direction, as seen in Fig. 12b.

The analogous response modes for  $Re = 60$  and  $Re = 180$  are plotted in Fig. 12c. Even though they scale with the Strouhal number  $St$  in Fig. 12d for a couple of periods, the profiles diverge further downstream. This can be attributed to the fact that  $U_c$  is not constant behind the cylinder (see Fig. 13a). As observed by Thompson et al. [40], the vortex street transitions from spaced-out vortices to a bunched-up street with more diffused vortices at a streamwise location of approximately  $x = 10$ .  $U_c$  is also calculated by tracking the local minima and maxima of the fluctuating  $v$  field in the DNS snapshots. The minima correspond to the edges of the vortices, and these results match the values obtained using the mode shape. It can be concluded that the most amplified global resolvent mode contains almost all of the dynamics of the flow.

### C. Recirculation and the Wave Maker

Figure 13a shows that  $U_c$  increases behind the cylinder before it either reaches a constant value in the low-Reynolds-number cases or attains a maximum before decreasing in the high-Reynolds-number cases. This implies that the vortices are accelerating after forming behind the cylinder. It also signifies that the wavelength of the resolvent response mode is constantly increasing as a function of streamwise distance. The initial wavelength is proportional to the recirculation length (see figure 11 of Ref. [41]) or the size of the vortex immediately before it is shed from the cylinder. Because there are two vortices of opposite signs per wavelength of the response mode, the initial wavelength is thus  $2l_m$ . The convection velocity at the recirculation point is consequently Reynolds-number dependent and is proportional to  $l_m\omega_s$ .

To achieve the convection velocity at  $x_r$ , the vortex needs to accelerate over a distance  $l_m$  from an initial speed of zero. Assuming the acceleration  $a$  is constant, which is a reasonable assumption because the slope of  $U_c$  in Fig. 13a [42] is also approximately constant at the beginning of the vortices' trajectory, simple kinematics can be used to determine acceleration, beginning with the following:

$$U_c = U_i + a\Delta t \quad (34)$$

where  $U_i$  is the initial velocity of the vortex and is set to zero. Equation (34) can be integrated to recover the displacement of the vortex, which is necessary for the next one to form, i.e.,  $l_m$ :

$$l_m = \frac{1}{2} a\Delta t^2 \quad (35)$$

$\Delta t$  can be eliminated from both equations to recover an equation for the final convection velocity  $U_c$  in terms of  $l_m$ :

$$U_c^2 = 2al_m \quad (36)$$

The final value of  $U_c$  is proportional to  $2l_m\omega_s$  because this is the wavelength of the resolvent response mode at  $x_r$ , and so acceleration scales in the following manner:

$$a \sim \omega_s^2 l_m \quad (37)$$

The value of the acceleration in Eq. (37) is the acceleration rescaled such that it is independent of the Reynolds number. The time scale associated with the vortices is  $\omega_s$ , whereas the length scale is  $\delta$ . Ignoring the fact that smaller vortices eventually slow down due to the decay of the von Kármán vortex street, the convection velocity is constant across Reynolds numbers sufficiently downstream of the cylinder. The length scale associated with the acceleration, on the

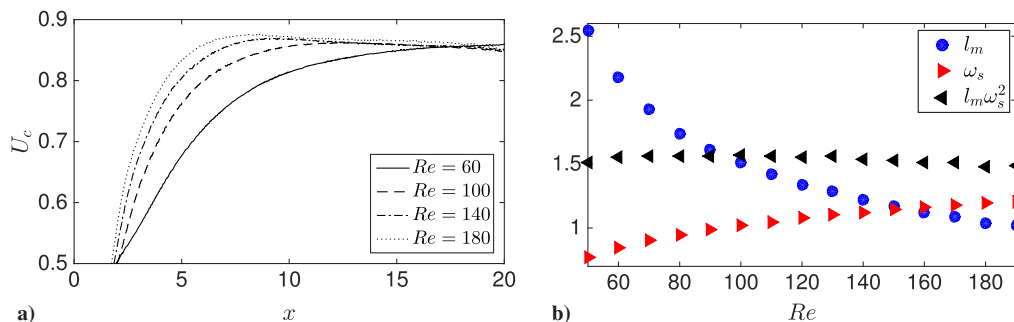


**Fig. 13** Representations of a)  $U_c$  of the vortices, which agree with Williamson [42]; and b) the relationship between  $l_m$  and  $\omega_s$ .

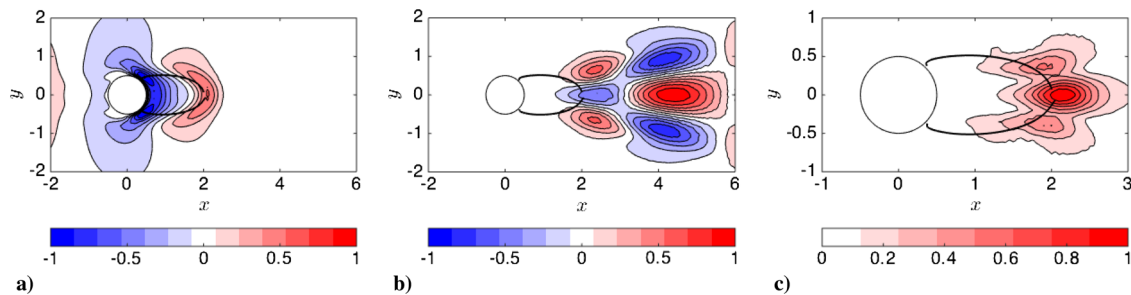


Fig. 14 Representations of a)  $\hat{\phi}_1(\omega_s)$ , b)  $\hat{f}(\omega_s)$ , and c) the magnitude of their overlap  $|\hat{\phi}_1(\omega_s)| |\hat{f}(\omega_s)|$  for  $Re = 100$ .

other hand, is  $l_m$  (or  $\delta$  immediately behind the cylinder), whereas the time scale is  $\omega_s$  because there are no other time scales in the flow. The maximum convection velocity given by  $\delta\omega_s$  is constant across all Reynolds numbers, whereas the acceleration  $l_m\omega_s^2$  is also constant. Consequently, there is a relationship between a mean quantity  $l_m$  and a frequency of fluctuation  $\omega_s$ . The respective values for  $l_m$ ,  $\omega_s$ , and  $l_m\omega_s^2$  are plotted in Fig. 13a to show  $l_m\omega_s^2$  is constant across Reynolds numbers.

The fact that  $l_m$  is directly related to the frequency of the unsteady fluctuations supports the notion that the wave maker  $\mathcal{W}$ , which can be approximated by

$$\mathcal{W}(x_0) \approx |\hat{\psi}_1(x_0, \omega_s)| |\hat{\phi}_1(x_0, \omega_s)| \quad (38)$$

(where  $|\cdot|$  denotes the magnitude) represents the region of instability in the flow (e.g., Giannetti and Luchini [43]). The wave maker is calculated using the resolvent singular vectors, which are identical to the eigenvectors of the LNS at the shedding frequency, because it is a resonant amplification mechanism [24]. In the present case, the length of the wave maker is equal to the recirculation bubble length  $l_m$ . A physical analogy can be noted between the bluff body flows and the simple pendulum. When visualizing contours of the streamwise velocity, there is a region of fluid (the length of which is approximately  $l_m$ ) with low streamwise velocity directly behind the cylinder, swinging up and down at a frequency of  $\omega_s$ . This is similar to a simple pendulum for which the radial frequency  $\Omega$  depends solely on its length  $L$  (i.e.,  $\Omega = \sqrt{g/L}$ ). Because  $g$  is a constant representing acceleration due to gravity, it can be shown that  $L\Omega^2$  is constant, which is analogous to  $l_m\omega_s^2$  for the cylinder flow.

#### D. Vortex Shedding and Nonlinear Forcing

We now consider how the vortex shedding is sustained by computing the Fourier transform of the nonlinear term  $\mathbf{u} \cdot \nabla \mathbf{u}$  at  $\omega_s$ , which is plotted in Fig. 14b alongside the optimal forcing mode in Fig. 14a. We know that this term is small because  $\mathbf{u}$  is predominately at  $\omega_s$ ; therefore,  $\mathbf{u} \cdot \nabla \mathbf{u}$  is predominately at zero and  $2\omega_s$ . The separation of singular values for this flow is significant ( $\sigma_1 \gg \sigma_2$ ), and so the projection of the nonlinear forcing at  $\omega_s$  onto the first forcing mode only is considered. It should be noted that the projection of  $\hat{f}(\omega_s)$  onto suboptimal modes is roughly equal to the first mode, and so the singular values result in the response being nearly proportional to  $\hat{\psi}_1$ . It is possible to visualize this projection in Fig. 14c and note that it occurs at the edge of the recirculation bubble. The overlap location is consistent across Reynolds numbers and reinforces the notion that the edge of the recirculation bubble coincides with the streamwise station of marginal absolute instability [44]. The wave-maker portion ahead of the overlap is the heart of the instability, and the rest of the flow convectively amplifies the perturbation (see Refs. [45,46]).

## VI. Minimum Number of Measurements for Complete Reconstruction

We may now capitalize on the physics and scaling from the previous section to identify where to measure the flow. The dynamically most significant region is arguably the downstream edge

of the wave maker, where the mean profile scales with the shedding frequency and the resolvent forcing mode overlaps with the nonlinear forcing. Some of the cases intentionally include or omit this region. Cases 2A and 2B are the minimum domain sizes ( $x \in [-2, 6] \cup y \in [-2, 2]$ ), where the artificial truncation of the experimental domain has a minimal impact on the reconstructed forcing. The cost functional for case 2A declines to 3.29% of the original value of cost functional A (recall that this is the same cost functional used for case 1A), whereas case 2B declines to 4.54% of the original value of cost functional B. Figures 15a–15c contain  $f_x$  for case 2A,  $f_x$  for case 2B, and  $f_y$  for case 2B, respectively. It does not include  $f_y$  for case 2A because it cannot be recovered from velocity-only measurements. All of the forcings match well with their full domain counterparts in Fig. 6. As such, they can be considered near the truth, against which the other cases can be compared.

#### A. Capturing the Wave Maker

Cases 3A and 3B include the wave-maker region ( $x \in [-1, 3] \cup y \in [-2, 2]$ ) but omit a portion of the flow where the pressure discrepancy between the base and mean flows is greatest. The data-assimilated velocity is close to the true mean for both cases 3A and 3B because cost functional A reaches 5.05% of its initial value. The pressure reconstruction is somewhat impacted as it declines to 6.56%. The truncation of the domain has a clear impact on the reconstructed forcings, which are plotted in Figs. 15d–15f. For case 3A,  $f_x$  agrees closely with the truth, despite truncating the domain behind  $x = 3$ . For case 3B, the effect of measuring only up until  $x = 3$  has a greater effect because the maximum  $f_x$  is concentrated at  $x > 3$  instead of  $x = 2.75$ . One can identify where measurements are available simply by looking at the spatial support of  $f_y$ , although the overall shape is in slightly better agreement with its DNS counterpart than  $f_x$ .

Cases 4A and 4B, where the domain is limited to  $x \in [-1, 2] \cup y \in [-2, 2]$ , are considerably worse because they do not capture the downstream edge of the wave maker. Cost functional A reaches 9.73% and B reaches 10.6%: values that are approximately a factor of two higher than the other cases. Moreover, the least stable eigenvalue predicted from a stability analysis is further from the truth than all the other cases (the real part is an order of magnitude higher), which do consider the entire wave-maker region. The problems associated with truncating the domain manifest themselves even more dramatically when plotting the forcing for these two cases as seen in Figs. 15g–15i. The spatial support of  $f_x$  and  $f_y$  is squeezed into a small region immediately behind the cylinder. To compensate, the algorithm overestimates the forcing amplitudes near the downstream edge of the measurement zone.

#### B. Nonlinear Forcing and Maximum Pressure Discrepancy

Limiting the domain to the region where the nonlinear forcing and optimal forcing modes overlap in cases 5A and 5B ( $x \in [1, 3] \cup y \in [-2, 2]$ ) is shown to be sufficient for reconstruction of the mean flow. Assimilation of the mean velocity is quite successful (the cost functional declines to 5.3%), but the mean pressure is less so (6.9%). Indeed, Figs. 15j–15l highlight how  $f_x$  is better reconstructed than  $f_y$  for this domain. Cases 6A and 6B limit the domain to where the initial pressure discrepancy  $p_0 - \bar{p}$  is

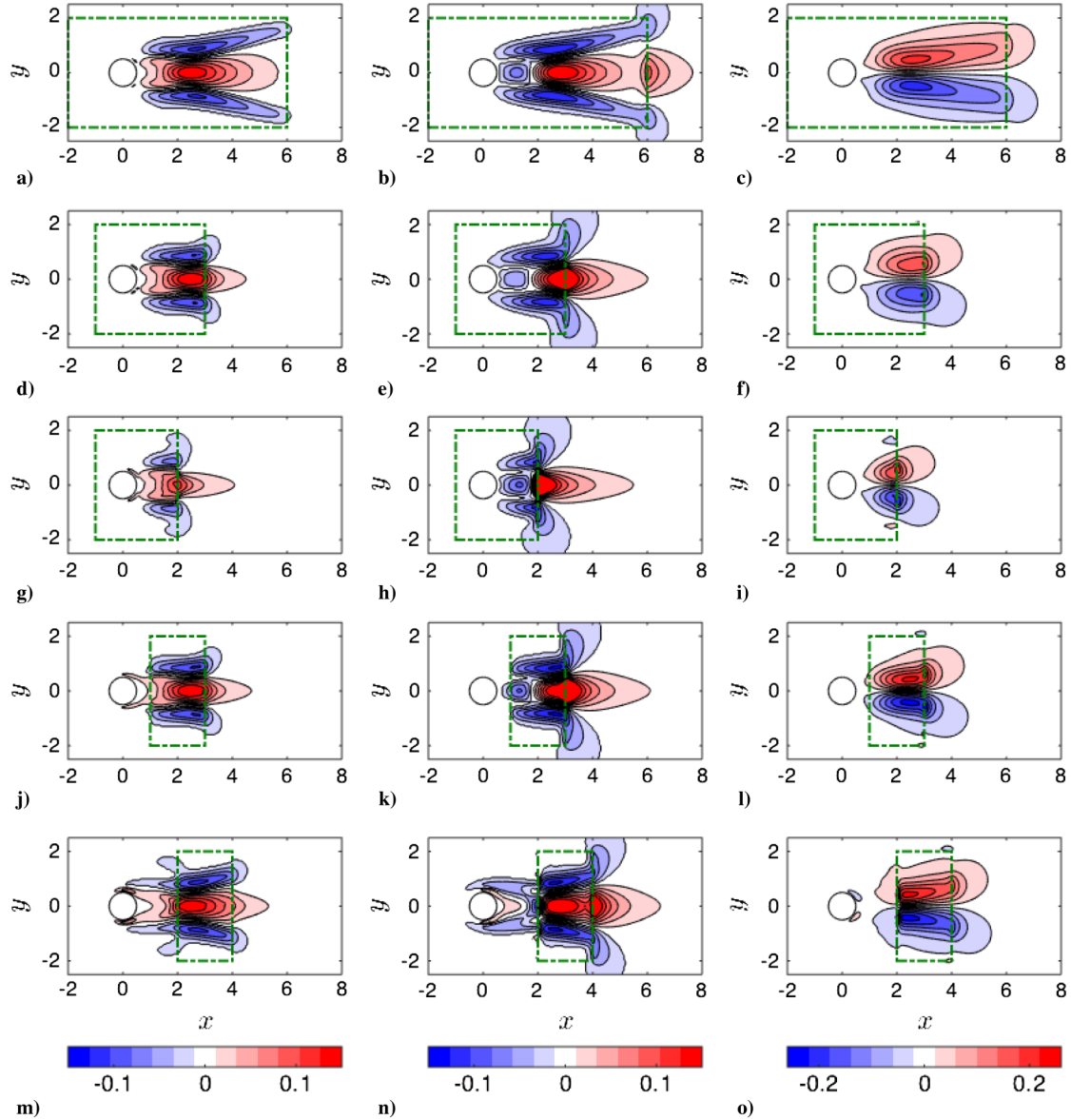


**Fig. 15**  $f_x$  (left) using velocity-only measurements,  $f_x$  (center) using velocity and pressure, and  $f_y$  (right column) using velocity and pressure for cases 2–6 (top to bottom). Green boxes indicate the domain where measurements are available.

greatest ( $x \in [2,4] \cup y \in [-2,2]$ ), and this yields improved pressure reconstruction (6.4%). The quality of the forcing, which is plotted in Figs. 15m–15o, is better for  $f_y$  than it is for  $f_x$ ; but, there is a qualitative improvement for both when compared to cases 5A and 5B. Measurement domains confined to the region upstream of the cylinder or in the far wake, which perform considerably worse than the cases considered here (see Ref. [15]), are not discussed in this paper.

It can be concluded that mean velocity measurements are most important at the edge of the wave maker, where the nonlinear forcing and resolvent forcing mode overlap. Additionally, as demonstrated in Ref. [27], a local stability analysis of the mean wake at the edge of the recirculation bubble predicts the frequency of the vortex shedding, signifying that it is essential for the data-assimilation algorithm to reproduce the profile at this particular streamwise location. The mean pressure, on the other hand, is most successfully recovered by obtaining pressure measurements where the discrepancy between the initial guess and the true mean velocity is greatest ( $x \in [2,4]$ ). There is no pressure equivalent to particle image velocimetry (PIV), which makes it difficult to obtain pressure measurements in the wake. An alternative method for reconstructing the mean pressure field using the data-assimilated mean velocity field and resolvent analysis is presented in Sec. VI.D.

### C. Point Weighting to Speed up the Algorithm

Thus far, domain truncation has been performed according to the physics revealed by resolvent analysis, but with all points in that domain given equal weight, and therefore importance. We now investigate whether weighting the points based on the physical and modeling insights of the previous sections can improve the efficiency of the procedure. The effect of weighting the measurements with weight  $\zeta$  such that  $\mathcal{E}'_A(\bar{\mathbf{u}}) = 1/2 \|\zeta(\bar{\mathbf{m}} - \mathcal{M}(\bar{\mathbf{u}}, \bar{\mathbf{p}}))\|_M^2$  in three ways is considered. In case 7, the points are weighted by the value of the wave maker computed from the DNS mean. In case 8, they are weighted by the modulus of the most amplified resolvent response mode computed from the DNS mean. Because the domain on which experimental measurements is known may not be large enough to compute global resolvent modes, case 9 considers the wave maker computed from the assimilated flow at each iteration of the optimization (it is referred to as “iterative” in Table 1). The wave maker for the zeroth iteration, for example, is computed from the leading resolvent modes of the base flow. As the recirculation region shrinks during the data-assimilation procedure, the wave maker also shrinks.

The functional  $\mathcal{E}'_A(\bar{\mathbf{u}})$  is plotted as a function of iteration for cases 1A, 1B, and 7–9 in Fig. 5. Although weighting the points is slightly beneficial in terms of the speed at which the assimilated field

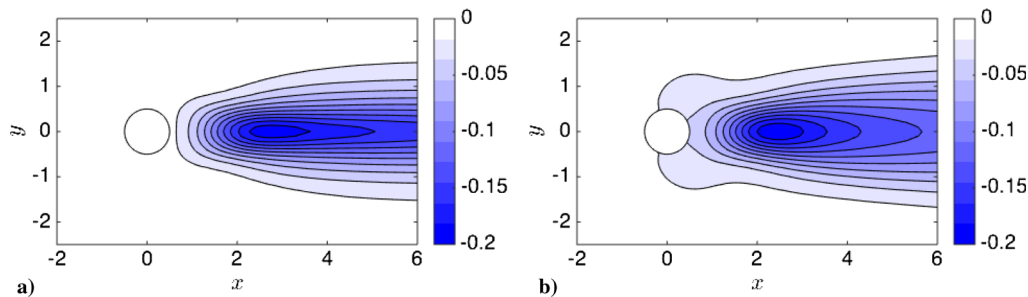


**Fig. 16** Representations of a) approximated mean pressure field discrepancy (i.e.,  $-\xi$ ), and b)  $\bar{p}_{\text{Case1}} - \bar{p}_{\text{DNS}}$ .

converges to the mean, there is no benefit in terms of the overall quality of the assimilation. Case 8 is arguably the best in terms of speed, which is reasonable because the Reynolds stresses can be approximated from the resolvent response modes. It can be concluded that the domain where experimental measurements is obtained is far more important than how points are weighted, which is encouraging because it is not necessary to redo the procedure once the weights are determined from the resolvent analysis of the data-assimilated mean.

#### D. Pressure Reconstruction

Because the global resolvent mode corresponding to  $\omega_s$  dominates the flow, the right-hand side of Eq. (26) can be approximated as the correctly weighted triadic interaction of  $\hat{\psi}_1(\omega_s)$  with its conjugate counterpart  $\hat{\psi}_1(-\omega_s)$ :

$$\nabla^2 \xi \approx -\nabla \cdot [2\text{Real}(\chi_1(\omega_s)\hat{\psi}_1(\omega_s) \cdot \chi_1(-\omega_s)\nabla\hat{\psi}_1(-\omega_s))] \quad (39)$$

The amplitude  $\chi_1(\omega_s)$  of the resolvent response mode is calibrated using knowledge of the fluctuating velocity field at a single point in the flow (e.g., Gómez et al. [1]). In this study,  $\tilde{v}(t)$  is measured at the point of  $\mathbf{x} = (2,0)$  to determine  $\chi_1(\omega_s)$ . Solving for  $\xi$  results in a pressure field that “corrects” the mean pressure computed from velocity-only data-assimilation. Reconstructing the unsteady pressure field can be accomplished from resolvent analysis by retaining the pressure term in the operator (e.g., Refs. [2,47]).

The approximated pressure discrepancy computed from solving Eq. (39) is compared with the discrepancy between cases 1A and 1B in Fig. 16. The agreement is surprisingly good, although the resolvent mode prediction is slightly narrower in the  $y$  direction. Another difference is that the resolvent prediction does not correct the mean pressure near the surface of the cylinder, and so it would not improve the mean pressure estimate of case 1A. Despite the success of this approach, the use of a single mode and frequency is unlikely to work as well for higher Reynolds numbers because Mantić-Lugo et al. [20] could not stabilize the cylinder wake using a single mode for  $Re > 110$ . Given the success of rank-1 models at predicting the spectra at various locations in the flow (e.g., Ref. [3]), it is possible to obtain an estimate of the Reynolds stresses that can be compared with the rotational forcing from velocity-only measurements. Regions of the flow where there is a difference between these two indicate where the mean pressure from the data-assimilation deviates from the true mean pressure.

## VII. Conclusions

The objective of this paper is to combine data-assimilation and resolvent analysis to reconstruct flows using as few measurements as possible. The procedure originally devised by Gómez et al. [1] and Beneddine et al. [3] is updated in Fig. 1 such that the mean profile obtained from undersampled experimental or simulation data can be recovered on a larger, more resolved mesh using data-assimilation. The improved mean velocity profile is the input to the resolvent analysis, and the calibrated resolvent modes are used to solve for mean pressure without directly measuring it. The advantage of this method is that it avoids having to compute gradients of Reynolds

stresses that amplify underlying noise in the experiment. It was also shown that both the scaling arguments and resolvent analysis can be used to guide the selection of measurement points. Even though the flows considered here are either periodic or quasi periodic, the procedure is capable of recovering the organized structures from experimental data at higher Reynolds numbers using a rank-1 model. This has been demonstrated for simulation data from turbulent flows in Ref. [3]. The spatially uncorrelated fluctuations, on the other hand, cannot be recovered [4].

Data-assimilation is performed for the mean flow around a circular cylinder at  $Re = 100$ . The measurements, which are an input to the algorithm, are varied by including or omitting pressure, truncating the domain where they were known, and weighting regions to emphasize important flow physics. It is concluded that the minimum measurements needed for successful reconstruction of an unsteady flow are mean velocity measurements in the domain where the Reynolds stresses are concentrated, as well as knowledge of the fluctuations at a single point to calibrate resolvent modes (more information might be available if the flow were Fourier transformed in space; e.g., Ref. [1]). Resolvent analysis identifies one dominant structure that is highly amplified at the shedding frequency even when the unsteady flow is three-dimensional. A Strouhal number based on the shedding frequency can collapse the profile of  $\sigma_1$  as a function of  $\omega$  and the mean profile at the recirculation point. The shedding frequency also manifests itself in the resolvent modes and the convection velocities of the shed vortices.

Immediately behind the cylinder, the wavelength of the resolvent response modes is proportional to the recirculation length. As they form behind the cylinder, the vortices accelerate in this region before they obtain their maximum convection velocity further downstream. The convection velocities of the vortices are thus shown to scale with the shedding frequency  $\omega_s$  and the wavelength  $\delta$ ; whereas the acceleration scales with  $\omega_s^2$  and the recirculation length  $l_m$ , establishing a link between  $\omega_s$ , the timescale of the fluctuations, and  $l_m$ , which is a statistical length. The optimal forcing mode overlaps with the nonlinear forcing at the recirculation point, which sustains the vortex shedding. The edge of the wave maker, therefore, is the most crucial region of the flow to obtain measurements for data-assimilation. When the measurement domain does not include this area, the algorithm performs significantly worse and the reconstructed solenoidal forcing cannot be accurately captured. For a generic flow, the domain needs to capture the Reynolds stress gradients. Because the amplified resolvent modes interacting with their complex conjugates form Reynolds stresses, a resolvent analysis of a very crude mean profile (e.g., interpolating the experimental mean onto a mesh or a Reynolds-averaged Navier–Stokes solution) could identify amplification mechanisms and their spatial support to guide the final particle image velocimetry domain. Weighting measurement points lead to a slightly faster rate of convergence but no meaningful improvement in the final result.

## Acknowledgments

The authors would like to acknowledge financial support from U.S. Air Force Office of Scientific Research grant number FA 9550-16-1-0361, Army Research Office grant number W911NF-17-1-0306, and Office of Naval Research grant number N0014-17-1-3022.

## References

- [1] Gómez, F., Blackburn, H. M., Rudman, M., Sharma, A. S., and McKeon, B. J., "A Reduced-Order Model of Three-Dimensional Unsteady Flow in a Cavity Based on the Resolvent Operator," *Journal of Fluid Mechanics*, Vol. 798, R2, June 2016. doi:10.1017/jfm.2016.339
- [2] Gómez, F., Sharma, A. S., and Blackburn, H. M., "Estimation of Unsteady Aerodynamic Forces Using Pointwise Velocity Data," *Journal of Fluid Mechanics*, Vol. 804, R4, Oct. 2016. doi:10.1017/jfm.2016.546
- [3] Beneddine, S., Sipp, D., Arnault, A., Dandois, J., and Lesshafft, L., "Conditions for Validity of Mean Flow Stability Analysis," *Journal of Fluid Mechanics*, Vol. 798, June 2016, pp. 485–504. doi:10.1017/jfm.2016.331
- [4] Beneddine, S., Yegavian, R., Sipp, D., and Leclaire, B., "Unsteady Flow Dynamics Reconstruction from Mean Flow and Point Sensors: An Experimental Study," *Journal of Fluid Mechanics*, Vol. 824, Aug. 2017, pp. 174–201. doi:10.1017/jfm.2017.333
- [5] Thomareis, N., and Papadakis, G., "Resolvent Analysis of Separated and Attached Flows Around an Airfoil at Transitional Reynolds Number," *Physical Review Fluids*, Vol. 3, No. 7, 2018, Paper 073901. doi:10.1103/PhysRevFluids.3.073901
- [6] Towne, A., Schmidt, O. T., and Colonius, T., "Spectral Proper Orthogonal Decomposition and Its Relationship to Dynamic Mode Decomposition and Resolvent Analysis," *Journal of Fluid Mechanics*, Vol. 847, July 2018, pp. 821–867. doi:10.1017/jfm.2018.283
- [7] Symon, S., "Reconstruction and Estimation of Flows Using Resolvent Analysis and Data-Assimilation." Ph.D. Thesis, California Inst. of Technology, Pasadena, CA, 2018. doi:10.7907/B4K7-K876
- [8] McKeon, B. J., and Sharma, A. S., "A Critical-Layer Framework for Turbulent Pipe Flow," *Journal of Fluid Mechanics*, Vol. 658, Sept. 2010, pp. 336–382. doi:10.1017/S002211201000176X
- [9] Rosenberg, K., "Resolvent-Based Modeling of Flows in a Channel," Ph.D. Thesis, California Inst. of Technology, Pasadena, CA, 2018. doi:10.7907/PHDW-Z389
- [10] Lewis, J. M., Lakshminarayanan, S., and Dhall, S., *Dynamic Data Assimilation: A Least Squares Approach*, *Encyclopedia of Mathematics and Its Application 104*, Vol. 13, Cambridge Univ. Press, New York, 2006.
- [11] Hayase, T., "Numerical Simulation of Real-World Flows," *Fluid Dynamics Research*, Vol. 47, No. 5, 2015, Paper 051201. doi:10.1088/0169-5983/47/5/051201
- [12] Le Dimet, F.-X., and Talagrand, O., "Variational Algorithms for Analysis and Assimilation of Meteorological Observations: Theoretical Aspects," *Tellus A*, Vol. 38A, No. 2, 1986, pp. 97–110. doi:10.3402/tellusa.v38i2.11706
- [13] Papadakis, N., and Mémin, E., "Variational Assimilation of Fluid Motion from Image Sequence," *SIAM Journal on Imaging Sciences*, Vol. 1, No. 4, 2008, pp. 343–363. doi:10.1137/080713896
- [14] Gronskis, A., Heitz, D., and Mémin, E., "Inflow and Initial Conditions for Direct Numerical Simulation Based on Adjoint Data Assimilation," *Journal of Computational Physics*, Vol. 242, June 2013, pp. 480–497. doi:10.1016/j.jcp.2013.01.051
- [15] Foures, D. P. G., Dovetta, N., Sipp, D., and Schmid, P. J., "A Data-Assimilation Method for Reynolds-Averaged Navier–Stokes-Driven Mean Flow Reconstruction," *Journal of Fluid Mechanics*, Vol. 759, Nov. 2014, pp. 404–431. doi:10.1017/jfm.2014.566
- [16] Symon, S., Dovetta, N., McKeon, B. J., Sipp, D., and Schmid, P. J., "Data Assimilation of Mean Velocity from 2-D PIV Measurements of Flow over an Idealized Airfoil," *Experiments in Fluids*, Vol. 58, No. 5, 2017, Paper 61. doi:10.1007/s00348-017-2336-8
- [17] Kang, W., and Xu, L., "Optimal Placement of Mobile Sensors for Data Assimilations," *Tellus A*, Vol. 64, Dec. 2012, Paper 17133. doi:10.3402/tellusa.v64i0.17133
- [18] Mons, V., Chassaing, J.-C., and Sagaut, P., "Optimal Sensor Placement for Variational Data Assimilation of Unsteady Flows Past a Rotationally Oscillating Cylinder," *Journal of Fluid Mechanics*, Vol. 823, July 2017, pp. 230–277. doi:10.1017/jfm.2017.313
- [19] Manohar, K., Brunton, B. W., Kutz, J. N., and Brunton, S. L., "Data-Driven Sparse Sensor Placement for Reconstruction," *IEEE Control Systems Magazine*, Vol. 38, No. 3, 2018, pp. 63–86. doi:10.1109/MCS.2018.2810460
- [20] Mantič-Lugo, V., Arratia, C., and Gallaire, F., "Self-Consistent Mean Flow Description of the Nonlinear Saturation of the Vortex Shedding in the Cylinder Wake," *Physical Review Letters*, Vol. 113, Aug. 2014, Paper 084501. doi:10.1103/PhysRevLett.113.084501
- [21] Provansal, M., Mathis, C., and Boyer, L., "Bénard-von Kármán Instability: Transient and Forced Regimes," *Journal of Fluid Mechanics*, Vol. 182, Sept. 1987, pp. 1–22. doi:10.1017/S0022112087002222
- [22] Sreenivasan, K. R., Strykowski, P. J., and Olinger, D. J., "Hopf Bifurcation, Landau Equation, and Vortex Shedding Behind Circular Cylinders," *Forum on Unsteady Flow Separation*, Vol. 1, American Soc. for Mechanical Engineers, Fluids Engineering Division, New York, June 1987, pp. 1–13.
- [23] Noack, B. R., and Eckelmann, H., "A Global Stability Analysis of the Steady and Periodic Cylinder Wake," *Journal of Fluid Mechanics*, Vol. 270, July 1994, pp. 297–330. doi:10.1017/S0022112094004283
- [24] Symon, S., Rosenberg, K., Dawson, S. T. M., and McKeon, B. J., "Non-Normality and Classification of Amplification Mechanisms in Stability and Resolvent Analysis," *Physical Review Fluids*, Vol. 3, No. 5, 2018, Paper 053902. doi:10.1103/PhysRevFluids.3.053902
- [25] Barkley, D., "Linear Analysis of the Cylinder Wake Mean Flow," *Europhysics Letters*, Vol. 75, No. 5, 2006, pp. 750–756. doi:10.1209/epl/i2006-10168-7
- [26] Barkley, D., and Henderson, R. D., "Three-Dimensional Floquet Stability Analysis of the Wake of a Circular Cylinder," *Journal of Fluid Mechanics*, Vol. 322, Sept. 1996, pp. 215–241. doi:10.1017/S0022112096002777
- [27] Leontini, J. S., Thompson, M. C., and Hourigan, K., "A Numerical Study of Global Frequency Selection in the Time-Mean Wake of a Circular Cylinder," *Journal of Fluid Mechanics*, Vol. 645, Feb. 2010, pp. 435–446. doi:10.1017/S0022112009993132
- [28] Hecht, F., "New Development in FreeFem++," *Journal of Numerical Mathematics*, Vol. 20, Nos. 3–4, 2012, pp. 251–265. doi:10.1515/jnum-2012-0013
- [29] Blackburn, H. M., and Sherwin, S. J., "Formulation of a Galerkin Spectral Element-Fourier Method for Three-Dimensional Incompressible Flows in Cylindrical Geometries," *Journal of Computational Physics*, Vol. 197, No. 2, 2004, pp. 759–778. doi:10.1016/j.jcp.2004.02.013
- [30] Sipp, D., and Marquet, O., "Characterization of Noise Amplifiers with Global Singular Modes: The Case of the Leading-Edge Flat-Plate Boundary Layer," *Theoretical and Computational Fluid Dynamics*, Vol. 27, No. 5, 2013, pp. 617–635. doi:10.1007/s00162-012-0265-y
- [31] Lehoucq, R. B., and Sorensen, D. C., "Deflation Techniques for an Implicitly Restarted Arnoldi Iteration," *SIAM Journal on Matrix Analysis and Applications*, Vol. 17, No. 4, 1996, pp. 789–821. doi:10.1137/S0895479895281484
- [32] Amestoy, P. R., Duff, I. S., L'Excellent, J.-Y., and Koster, J., "A Fully Asynchronous Multifrontal Solver Using Distributed Dynamic Shedding," *SIAM Journal on Matrix Analysis and Applications*, Vol. 23, No. 1, 2001, pp. 15–41. doi:10.1137/S0895479899358194
- [33] McKeon, B. J., Sharma, A. S., and Jacobi, I., "Experimental Manipulation of Wall Turbulence: A Systems Approach," *Physics of Fluids*, Vol. 25, No. 3, 2013, Paper 031301. doi:10.1063/1.4793444
- [34] Moarref, R., Sharma, A. S., Tropp, J. A., and McKeon, B. J., "Model-Based Scaling of the Streamwise Energy Density in High-Reynolds-Number Turbulent Channels," *Journal of Fluid Mechanics*, Vol. 734, Nov. 2013, pp. 275–316. doi:10.1017/jfm.2013.457
- [35] Williamson, C. H. K., "The Natural and Forced Formation of Spot-Like 'Vortex Dislocations' in the Transition of a Wake," *Journal of Fluid Mechanics*, Vol. 243, Oct. 1992, pp. 393–441. doi:10.1017/S0022112092002763
- [36] Williamson, C. H. K., "The Existence of Two Stages in the Transition to Three-Dimensionality of a Cylinder Wake," *Physics of Fluids*, Vol. 31, No. 11, 1988, Paper 2742. doi:10.1063/1.866925
- [37] Williamson, C. H. K., and Roshko, A., "Measurements of Base Pressure in the Wake of a Cylinder at Low Reynolds Numbers," *Zeitschrift für*

- Flugwissenschaften und Weltraumforschung*, Vol. 14, No. 1, 1990, pp. 38–46.
- [38] Henderson, R. D., “Details of the Drag Curve Near the Onset of Vortex Shedding,” *Physics of Fluids*, Vol. 7, No. 9, 1995, pp. 2102–2104. doi:10.1063/1.868459
- [39] Schmid, P. J., and Henningson, D. S., *Stability and Transition in Shear Flows*, Springer, New York, 2012.
- [40] Thompson, M. C., Radi, A., Rao, A., Sheridan, J., and Hourigan, K., “Low-Reynolds-Number Wakes of Elliptical Cylinders: From the Circular Cylinder to the Normal Flat Plate,” *Journal of Fluid Mechanics*, Vol. 751, July 2014, pp. 570–600. doi:10.1017/jfm.2014.314
- [41] Balachandar, S., Mittal, R., and Najjar, F. M., “Properties of the Mean Recirculation Region in the Wakes of Two-Dimensional Bluff Bodies,” *Journal of Fluid Mechanics*, Vol. 351, Nov. 1997, pp. 167–199. doi:10.1017/S0022112097007179
- [42] Williamson, C. H. K., “Oblique and Parallel Modes of Vortex Shedding in the Wake of a Circular Cylinder at Low Reynolds Numbers,” *Journal of Fluid Mechanics*, Vol. 206, Sept. 1989, pp. 579–627. doi:10.1017/S0022112089002429
- [43] Giannetti, F., and Luchini, P., “Structural Sensitivity of the First Instability of the Cylinder Wake,” *Journal of Fluid Mechanics*, Vol. 581, June 2007, pp. 167–197. doi:10.1017/S0022112007005654
- [44] Pier, B., “On the Frequency Selection of Finite-Amplitude Vortex Shedding in the Cylinder Wake,” *Journal of Fluid Mechanics*, Vol. 458, May 2002, pp. 407–417. doi:10.1017/S0022112002008054
- [45] Chomaz, J. M., Huerre, P., and Redekopp, L. G., “Bifurcations to Local and Global Modes in Spatially Developing Flows,” *Physical Review Letters*, Vol. 60, No. 1, 1988, pp. 25–28. doi:10.1103/PhysRevLett.60.25
- [46] Monkewitz, P. A., “The Absolute and Convective Nature of Instability in Two-Dimensional Wakes at Low Reynolds Numbers,” *Physics of Fluids*, Vol. 31, No. 5, 1988, pp. 999–1006. doi:10.1063/1.866720
- [47] Luhar, M., Sharma, A. S., and McKeon, B. J., “Opposition Control Within the Resolvent Analysis Framework,” *Journal of Fluid Mechanics*, Vol. 749, June 2014, pp. 597–626. doi:10.1017/jfm.2014.209

K. Taira  
Associate Editor